Materials Science and Engineering A 534 (2012) 220–227

Contents lists available at SciVerse ScienceDirect

Materials Science and Engineering A

journal homepage: www.elsevier.com/locate/msea

Prediction of bulk tensile behavior of dual phase stainless steels using constituent behavior from micropillar compression experiments

J.L. Stewart, L. Jiang, J.J. Williams, N. Chawla*

Arizona State University, Tempe, AZ 85287-6106, United States

ARTICLE INFO

Article history:
Received 18 July 2011
Received in revised form 27 October 2011
Accepted 9 November 2011
Available online 1 December 2011

Keywords:
Micropillar compression
Powder metallurgy steel
Nanoindentation

ABSTRACT

Micropillar compression has become an attractive method to probe local mechanical behavior. While most micropillar compression work has focused on investigating size effects, we can also use this technique to obtain the constitutive behavior of microscopic phases and constituents. In this study, micropillars of ferrite and martensite were fabricated by focused ion beam (FIB) milling of dual phase precipitation hardened powder metallurgy (PM) stainless steels. Compression testing was conducted using a nanoindenter equipped with a flat punch indenter. The stress–strain curves of the individual microconstituents were obtained. Using a rule of mixtures approach in conjunction with porosity corrections, the mechanical properties of ferrite and martensite were combined to predict the tensile behavior of the bulk material, and reasonable agreement was found for the ultimate tensile strength.

1. Introduction

Powder metallurgy (PM) offers many advantages including applicability to a wide variety of alloying systems, production of complex shapes, part to part uniformity, long term performance reliability, minimal scrap loss, and cost effectiveness [1]. Similar to wrought counterparts, PM parts can be produced with a wide variety of microstructures to tailor mechanical behavior and may be heat treated for increased strength and/or wear resistance. However, the early onset plasticity and localization of strain due to reduction of the load bearing cross-sectional area [2] and the stress concentration effect of angular pores [3] are detrimental to the mechanical properties of porous materials. Several authors have developed relationships to relate strength to porosity [4–11] with limited universal success due to the complex nature of porosity and its effects on the surrounding matrix microstructure.

The increasing demand for high strength PM steels has led to the development of dual phase PM stainless steels [12]. The dual phase steel microstructure consists of both martensite and ferrite microconstituents and is achieved through the use of austenite and ferrite stabilizers in the alloy coupled with specific processing conditions. In addition, low carbon concentration in the alloy is necessary to coincide with the two phase austenite–ferrite region of the Fe–C phase diagram. At high temperatures, the steel is composed of ferrite and austenite but upon cooling, the austenite converts to martensite and the dual phase ferrite–martensite microstructure is achieved. This transformation is known to cause a high dislocation density in the ferrite near martensite–ferrite interfaces [12–14] and high residual stresses [14–16]. Because of the complex microstructures and mechanisms involved, dual phase steels are known to exhibit continuous yielding behavior, high work hardening rate, low yield strength, and high ultimate tensile strength [17]. Dual phase steels also benefit from their composite microstructure in that the martensite imparts strength while ferrite imparts ductility. Hence, the mechanical properties of the steel may be tailored by varying the phase fractions of each constituent. By conventional composite strengthening, as the fraction of the harder phase, in this case martensite, is increased, the strength of the composite is increased. Several rule of mixtures relationships have been developed to describe the mechanical behavior of the composite microstructure based on the phase fractions and mechanical properties of the microconstituents [18–20].

Understanding the contributions of the individual microconstituents to the mechanical behavior of dual phase steels has proven difficult due to inability to obtain accurate constitutive relationships of each individual constituent. The properties of martensite or ferrite in bulk form are not representative of their behavior at the microscale. Conventional nanoindentation using a sharp tip Berkovich indenter has been used to probe the local mechanical properties of dual phase steels [21–24] but is limited to the determination of the Young's modulus and hardness of the microconstituents. Due to confinement of plastic deformation to a very small volume, non-uniform strain and stress distributions result during indentation. So-called indentation size effects are attributed to these strain gradients as addressed by strain gradient theory [25]. Furthermore, contributions from surrounding features, such

* Corresponding author. Tel.: +1 480 965 2402; fax: +1 480 727 9321.
E-mail address: nchawla@asu.edu (N. Chawla).

0921-5093/$ – see front matter © 2011 Elsevier B.V. All rights reserved.
doi:10.1016/j.msea.2011.11.062

Table 1
Nominal powder composition of 1% Cu DPPH alloy (wt.%).

C	P	Si	Cr	Ni	Cu	Mn	Mo	Fe
0.013	0.012	0.83	12.11	1.06	0.99	0.07	0.38	Balance

as mutual constraint between two phases or grain boundary effects, cannot be removed from conventional nanoindentation experiments. Novel and creative techniques must be used to quantify the constitutive behavior of individual microconstituents.

Micropillar compression of microsized pillars is a promising technique for obtaining the stress–strain behavior at small-length scales. The technique consists of the fabrication of free-standing pillars in the micron to nanometer scale, which can be isolated to individual phases, followed by compression using a nanoindenter with a flat punch. For the most part, this technique has been used to study size effects on mechanical properties [26–33] of single crystal materials. In addition, Jiang and Chawla [34] have used the technique to obtain the constitutive behavior of intermetallic phases formed in Sn-based alloys. Most applicable to the current study, Pouchon et al. [35] performed micropillar compression studies of irradiated oxide dispersion strengthened (ODS) ferritic steel alloys and compared micropillar compression results to those of tensile tests with reasonable success.

In this study, micropillar compression was employed to determine the mechanical properties of individual microconstituents in a PM-processed dual phase steel. Furthermore, this testing was conducted on both as-sintered and thermally aged specimens to gain an understanding of the effect of aging on deformation behavior. Using a modified rule-of-mixtures approach for dual phase steels, the composite behavior of the steel was quantified. The constitutive behavior of the phases developed from micropillar compression was coupled with existing strength–porosity models from the literature to predict the ultimate tensile strength of the steel. Direct comparisons of the predictions with tensile tests of the bulk dual phase steel were conducted and the correlations were quite good.

2. Materials and experimental procedure

The specimens used in this study were processed by Hoeganaes Corporation. The nominal composition of the dual phase precipitation hardened (DPPH) steel alloy is shown in Table 1. The powders were mixed with 0.75 wt.% of an organic binder (Acrawax C, Promaplast, Mexico) and compacted at 386 MPa into standard rectangular shapes with gage and total lengths of approximately 38 mm and 86 mm, respectively. The samples were sintered for 30 min at 1260 °C in hydrogen to a density of 6.60 g/cm^3. After cooling, five specimens were aged in 100% nitrogen for 1 h at a temperature of 538 °C and were cooled to room temperature. Five as sintered specimens were also retained. Tensile testing was conducted at a nominal displacement rate of 0.01 mm/s.

The as-sintered and aged specimens were cross-sectioned and polished to a final 0.05 μm silica finish. The porosity was characterized at three regions in each sample using optical microscopy followed by digital image analysis. Kalling's Reagent #1 (1.5 g $CuCl_2$, 33 mL HCl, 33 mL ethanol, 33 mL water) was used as an etchant to distinguish ferrite and martensite. This etchant colors the ferrite phase and etches the martensite [36]. The specimens were etched by swabbing with the etchant for 4 min immediately after final polishing. Three microstructurally representative regions of each specimen were imaged using optical microscopy and phase fractions were determined by manually shading the ferritic regions. Image processing by segmentation of the shaded images yielded the ferrite fraction. The martensite fraction was calculated by subtracting the ferrite fraction from the total area excluding the porous regions.

Micropillars were fabricated in both the ferrite and martensite phases of the as sintered and aged specimens using a focused ion beam (FEI FIB/SEM Nova 200, Hillsboro, OR). These pillars were fabricated in two steps. First, a rough pillar with a surrounding 20 μm trench was formed using a voltage and current of 30 kV and 5 nA, respectively. The resulting pillar structure was of relatively large diameter (4 μm). A second pass was conducted at a lower current (0.3 nA) and resulted in pillar diameters of ~1.5 μm and heights of ~4 μm. The final pillars exhibited a slight taper of approximately 5–6° so the aforementioned pillar diameter is representative of the diameter at the top surface of the pillar. Effort was taken to maintain similar pillar volumes and dimensions for all fabricated pillars. To accomplish this, different milling dimension parameters on the second pass were necessary for the ferrite and martensite phases. The effect of ion beam damage from Ga^+ ion implantation was assumed negligible since previous studies have estimated it to be no more than 60 nm at 30 kV under normal incidence [30,37] which is significantly less than the pillar dimensions and compression displacement used here.

The micropillars were compressed using a commercial nanoindenter (Nanoindenter XP-II, Agilent) equipped with a Berkovich three-sided pyramid diamond indenter with a flat tip. This tip had a flat triangular cross-section with a 10 μm side, thus having adequate surface area to accommodate the entire pillar diameter. The formation of the 20 μm trench around the pillars in the previous milling steps prevented the indenter from contacting the surrounding material and allowed for easy location of the pillars. A continuous stiffness measurement (CSM) technique was used in all experiments [38]. This technique consists of applying a small harmonic, high frequency amplitude during indentation loading, and measuring the contact stiffness of the sample from the displacement response at the excitation frequency. The main advantage of the CSM technique is that the contact stiffness can be measured instantaneously as a function of indentation depth. A displacement of 1000 nm was used for all pillar compression experiments. The resulting load–displacement curves were converted to stress–strain plots by the method of Greer et al. Here it is assumed that plastic volume is conserved upon loading the cylindrical pillar [28]. After deformation, fractographic analysis of the pillars was conducted on the pillars using a dual beam FIB equipped with a scanning electron microscope (SEM).

3. Results and discussion

3.1. Microstructure

Quantitative analysis of pore fraction, as well as phase fractions of ferrite and martensite were conducted. Representative optical micrographs of the steel's porosity are shown in Fig. 1. Porosity levels for the as-sintered and aged (at 538 °C) specimens were determined to be 26.6 ± 0.8% and 27.3 ± 0.4%, respectively. Clearly, porosity does not vary significantly with aging temperature. The tortuous nature and size of the pores are also consistent between the two aging conditions. Porosity primarily affects mechanical behavior by reducing the load-bearing cross-sectional area [2] and introducing stress-concentrators at irregularly shaped pores leading to early onset of plasticity and localization of strain [3]. Porosity may also affect the local cooling rates of the material leading to differences in microstructure and mechanical behavior [24].

The microstructure was studied further by etching the polished surfaces. The dual phase microstructures containing both ferrite and martensite, in both the as-sintered and aged specimens, are clearly seen, Fig. 2. This microstructure is achieved through the

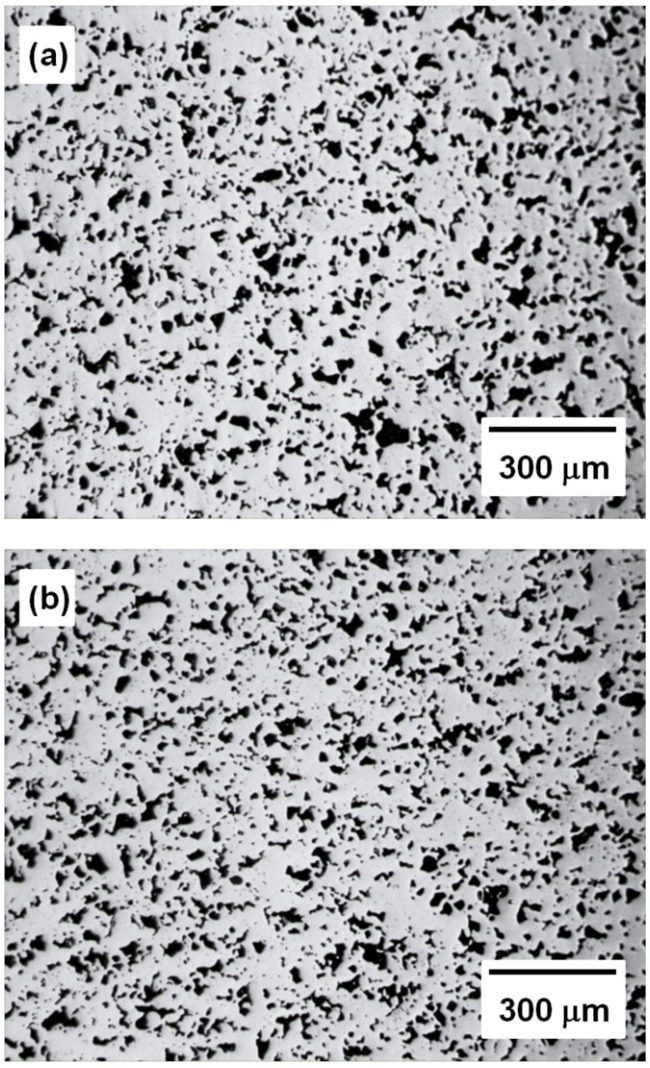

Fig. 1. Optical micrographs showing similar porosity for the: (a) as sintered and (b) aged at 538 °C specimens.

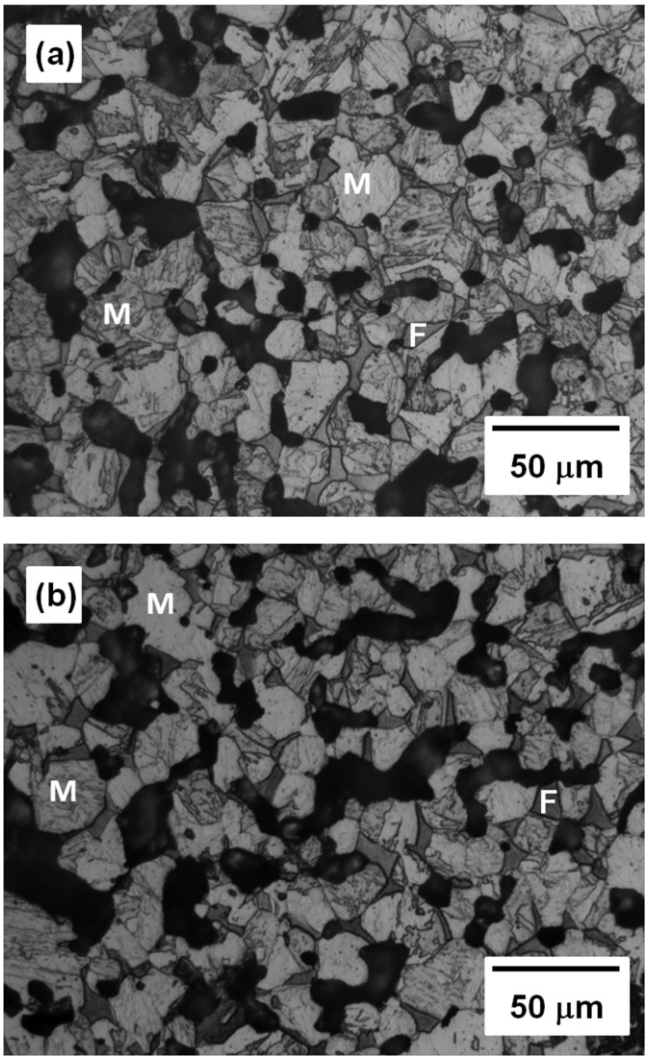

Fig. 2. Optical micrographs of: (a) as sintered and (b) aged at 538 °C specimens etched with Kalling's Reagent No. 1. Ferrite and martensite are labeled with F and M, respectively. Note similar phase fractions for as sintered and aged specimens.

use of specific alloying elements and processing conditions. The nominal steel composition consists of ferrite stabilizers (chromium, silicon, and molybdenum) and austenite stabilizers (nickel and copper) in the alloy. These stabilizers alter the ferrite–austenite region on the Fe–C phase diagram in support of the development of the dual phase microstructure. Also, at the sintering temperature of 1260 °C, the alloy is in the two phase ferrite–austenite region due to the low carbon concentration of the steel. Upon rapid cooling, the austenite in the steel transforms to martensite. It is not uncommon for austenite to be retained in the structure upon cooling. However, in low carbon steels, such as that studied here, the amount of retained austenite has been shown to be near zero after quenching due to a martensite finish temperature, M_f, above room temperature [39]. Austenite was not observed in our microstructural analysis and was assumed to be below the detection limits of typical X-ray diffraction techniques.

The phase fractions of ferrite and martensite content were approximately 8% and 92%, respectively. The measured phase fractions were identical for both as-sintered and aged specimens. Optical microscopy also showed no significant microstructural differences in grain size and shape, tempered martensite appearance, etc., between the as-sintered and aged specimens. This finding is consistent with previous studies of high strength low alloy steel subjected to thermal aging [40]. It should be noted that while the phase fractions do not appear to change with aging temperature, it is possible that local diffusion and relief of residual stresses may be taking place, so that the local mechanical properties might be changing with aging temperature. Precipitates are also presumed to form upon aging but are not detectable by optical microscopy due to its limited resolution. Previous studies showed very small copper precipitates, approximately 10–50 nm in size, which were only detectable by transmission electron microscopy, in steels of similar composition and aging conditions [40,41]. Copper precipitates are expected to grow in size with thermal aging of the steel.

3.2. Mechanical behavior of the bulk steels from tensile testing

Tensile stress–strain curves of the as-sintered and aged specimens show continuous yielding behavior and the lack of defined yield points consistent with dual phase steels (Fig. 3). This behavior has been attributed to high mobile dislocation density in the ferrite near martensite interfaces [13,14] and high residual stresses resulting from the inherent volume expansion associated with the austenite to martensite transformation [14–16]. Upon loading, early plastic flow is observed due to the movement of these mobile dislocations and flow continues in the ferrite due to its

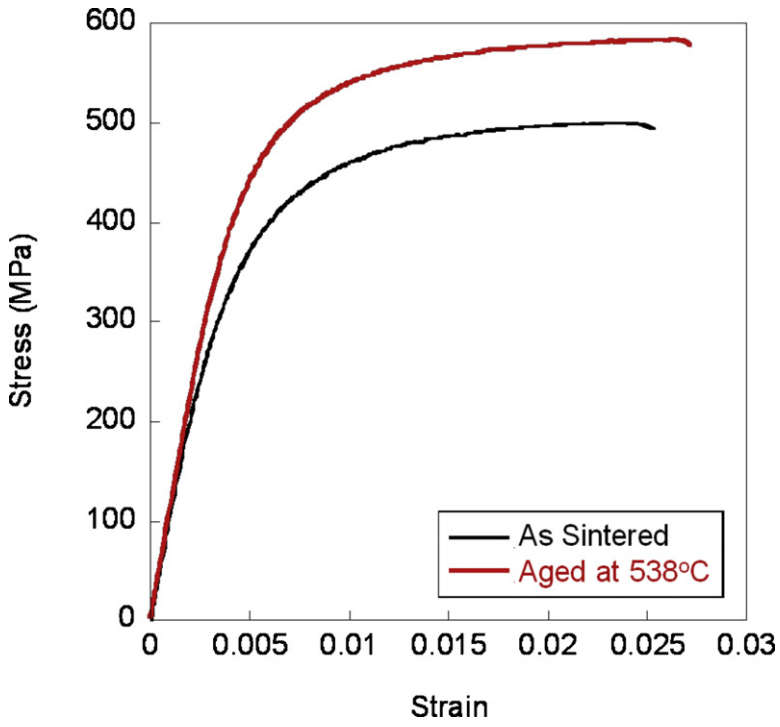

Fig. 3. Example of as sintered and aged specimens' stress vs. strain curves showing continuous yielding and increased strength with aging.

lower yield strength. Once this phase is significantly strained, the martensite begins to deform and deformation continues in both phases simultaneously. Early plastic flow may also result from localization of strain due to the irregular pore shape or inhomogeneous pore distribution. Irregular pore shape causes high stress concentration at pores which results in localized slip leading to crack initiation [42,43]. This is expected to increase with increasing hardness of the matrix material. Clustering of the pores is representative of inhomogeneous distribution of pores in the material and results in areas of higher than average porosity at which fracture may then occur preferentially by crack propagation and/or void coalescence between closely neighboring pores. Furthermore, plasticity has been shown to initiate at pore clusters due the higher localized stress intensity associated with these defects [44–46].

The ultimate tensile strengths and yield strengths (as 0.2% offset) of the as-sintered and aged specimens are shown in Table 2. Young's modulus and strain-to-failure were also determined [24] but are beyond the scope of this work and are therefore not discussed here. Increases in both the yield strength and ultimate tensile strength are observed with aging. These trends presumably result from the precipitation hardening response of copper in the alloys. During aging, fine precipitates form in both the ferrite and martensite. We focus our attention on the precipitation of copper due to the low carbon and nitrogen contents of this steel. As aging temperatures are increased from the as-sintered condition to 538 °C, the supersaturated solution decomposes and copper precipitates grow in size. Dislocation mobility is impeded and the alloy resists deformation. Reductions in residual internal stresses likely also contribute to increased strength.

Table 2
Tensile testing of as sintered and aged specimens.

Aging temperature	σ_{UTS} (MPa)	σ_{YS} (MPa)	E (GPa)	Strain-to-failure (%)
As-sintered	509 ± 12	394 ± 10	116 ± 3	2.6 ± 0.3
538 °C	588 ± 4	487 ± 2	116 ± 3	2.8 ± 0.1

3.3. Micropillar compression

Stress–strain plots for the individual microconstituents were obtained by micropillar compression. The top diameter of the pillar was used to calculate the nominal cross-sectional area of the pillars as in previous studies [33,47]. The strain was calculated as the ratio of the measured displacement to the original pillar height less its plastic compressive displacement (expressed as a percentage). The method of Greer et al. [28] was used to correct the stress–strain curve, whereby the pillars are assumed to be perfectly cylindrical and the volume during plastic deformation is assumed to be conserved during compression. The resulting stress–strain curves are shown in Fig. 4. Two tests for each microconstituent per aging condition were completed. A summary of the compressive properties is shown in Table 3.

As expected, micropillar compression tests show higher strengths for martensite when compared to ferrite. The effect of aging is also examined. The yield strength of ferrite is observed to increase with aging temperature, while the fracture strength remains relatively constant. It is arguable that both the yield and fracture strengths of ferrite are within test scatter and therefore may be considered to remain constant with aging. Martensite, however, exhibits both increased yield and fracture strengths with aging which is consistent with results from tensile tests of the composite dual phase bulk specimens. This increased strength with aging is attributed to the growth of copper containing precipitates which hinder dislocation motion by mechanisms such as Orowan bowing [24]. It is therefore concluded that martensite is the primary driver of increased strength with aging in the bulk, especially

Table 3
Yield and fracture strengths of ferrite and martensite from micropillar compression.

Aging temperature	Yield strength (MPa)		Fracture strength (MPa)	
	Ferrite	Martensite	Ferrite	Martensite
As-sintered	569 ± 8	887 ± 53	823 ± 40	1475 ± 143
538 °C	610 ± 151	1177 ± 54	808 ± 146	1858 ± 348

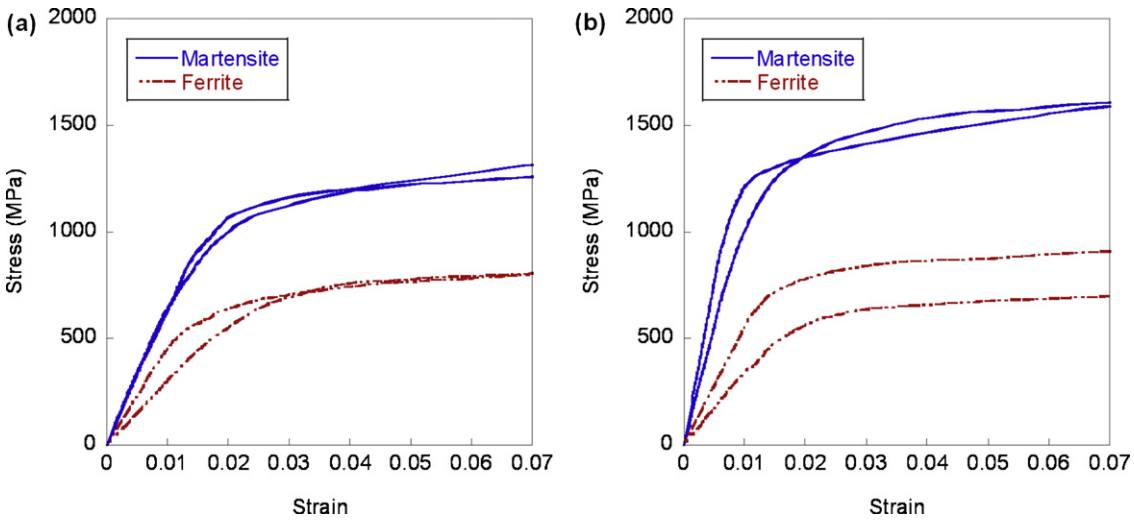

Fig. 4. Stress–strain curves from ferrite and martensite micropillar compression of: (a) as sintered and (b) aged at 538 °C specimens. Note increased martensite strength with aging.

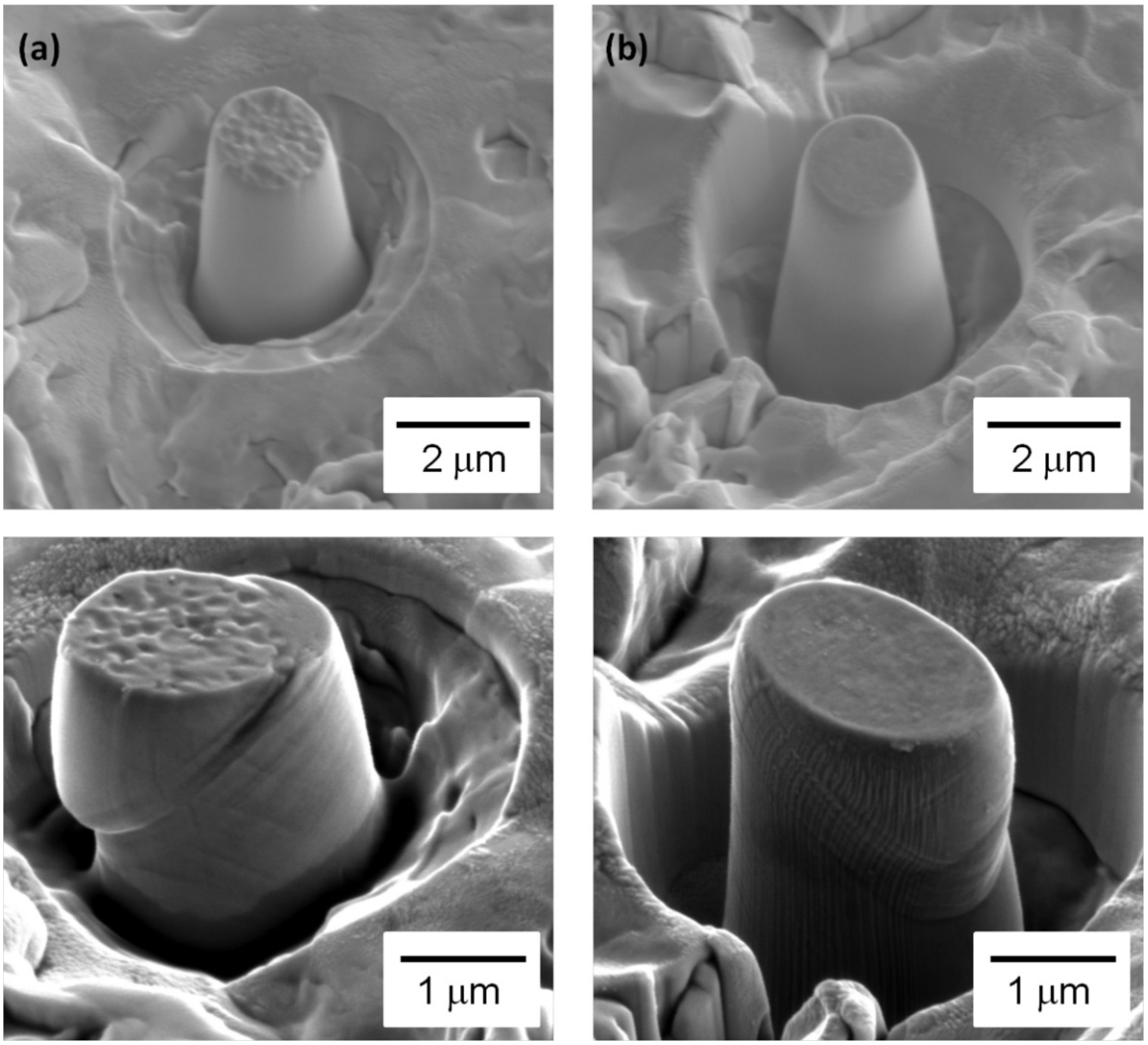

Fig. 5. Scanning electron microscope images of: (a) ferrite and (b) martensite pillar pre and post deformation. Note pillar deformation occurs by crystallographic slip.

with its predominate martensite phase fraction of 92%. Micrographs of representative pillars in ferrite and martensite (pre and post-deformation) are shown in Fig. 5. Nearly constant initial volumes and dimensions were maintained for all fabricated pillars. Deformation is observed to occur by crystallographic slip.

Much of the work on micropillar compression has focused on size effects observed in single crystal materials, in which increased strength is noted with decreased pillar size due to dislocation starved conditions [26–29,31–33]. In the current work, the objective was to obtain the constitutive stress–strain behavior of the individual microconstituents, and not to investigate size effects. As such, the volumes tested here are likely large enough to be in the regime where size effects do not play a role since the current pillar diameter is greater than the critical diameter of approximately 1 μm previously noted [29]. In addition, the steel studied here is not expected to suffer from size effects due to its inherent defect and dislocation density. Pouchon et al. [35], in fact, observed good agreement in the yield stresses measured by tensile testing and micropillar compression tests of irradiated ferritic steel and therefore concluded that size effects were not present in the material. This absence of the size effect was attributed to the presence of defects in the material. It should also be noted that Pouchon's pillars were of similar diameter to the pillars investigated here.

3.4. Using stress–strain data from microconstituents to predict bulk behavior

In this section we aim to incorporate the microconstituent stress–strain response from micropillar compression experiments to predict the bulk tensile behavior. Even though the experiments were conducted in compression, we assume here that there is very little asymmetry between tensile and compressive behavior of the pillars, particularly since the pillars are fully-dense. It is necessary to apply a rule of mixtures model to translate the microconstituents' properties into composite properties of the bulk steel. Due to the inherent differences in mechanical behavior of the microconstituents, many authors have considered various rule of mixtures relationships to describe the mechanical behavior of dual phase steels of varying phase fraction [18–20]. Speich and Miller [18] worked under the assumption that gross flow in martensite does not occur until the ultimate tensile strength of the ferrite is reached, and therefore the ultimate strength of the composite is represented by:

$$S_u = S_{m,0.2\%}V_m + S_{f,u}V_f$$

where S_u is the ultimate tensile strength of the composite, $S_{m,0.2\%}$ is the 0.2% offset yield strength of martensite, $S_{f,u}$ is the ultimate tensile strength of ferrite, and V_m and V_f are the phase fractions of martensite and ferrite, respectively. This relationship operates under the traditionally held idea that ferrite imparts ductility while martensite imparts strength in dual phase steels. Tamura et al. [19] assumed that deformation in dual phase steels occurs somewhere between isostrain and isostress conditions and considered that engineering stress and strain are partitioned between the two phases as given by:

$$S = S_fV_f + S_mV_m$$
$$\varepsilon = \varepsilon_fV_f + \varepsilon_mV_m$$

where S_f and S_m are the engineering stresses in ferrite and martensite, respectively, while ε_f and ε_m are the engineering strains. Since it is unlikely that the strains in the ferrite and martensite will be in a fixed ratio throughout deformation due to their differing mechanical properties, Rios et al. [20] expanded on this idea and developed a relationship to further describe the partitioning between the phases. It was assumed that the steel deforms uniformly up to the onset of plasticity due to similar elastic moduli of the microconstituents, after which variations in stresses in the ferrite and martensite are approximated to behave in a linear fashion. Thus, the stress in the martensite, S_m, is given by:

$$S_m = S_{f,y}\frac{S_{f,u} - S_{m,0.2}}{S_{f,u} - S_{f,y}} + S_f\frac{S_{m,0.2} - S_{f,y}}{S_{f,u} - S_{f,y}}$$

where $S_{f,y}$ is the yield stress of ferrite. Therefore, if the stress–strain behavior of the ferrite and martensite are known, the stress–strain curve of the composite dual phase steel may be calculated by solving for S_m and substituting into Tamura's relationship for stress of the steel. The strains from the ferrite and martensite compression tests are used in Tamura's equation for total strain. In the current study, it is expected that the ferrite fraction is too low to solely support early deformation and thus ferrite and martensite will simultaneously deform. Therefore, we utilize a conventional rule of mixtures model, like that given by Tamura, to obtain the fracture strengths and stress–strain curves for the composite microstructure (Fig. 6).

Using the ferrite and martensite fracture strengths from micropillar compression (Table 3), the fracture strengths of the as-sintered and thermally aged dual phase steels were found to be 1420 MPa and 1770 MPa, respectively. These strengths are representative of the fully dense composite microstructure since all pillars are assumed to be non-porous.

The bulk tensile tests are inclusive of the steel's porosity (~27%) and therefore the aforementioned rule of mixtures results must be adjusted for porosity since porosity significantly affects strength. Several relationships for strength as a function of porosity have previously been developed but with difficulty due to oversimplification of pore shape, morphology, and distribution. These relationships are also confounded by the effect of porosity on microstructure. As a result, it is nearly impossible to develop a universal strength–porosity equation that is applicable to all materials. We therefore present a review of select strength–porosity relationships for sintered iron compacts from the literature. For all equations, σ is the tensile strength of the porous material, σ_0 is the tensile strength of the fully dense material, and p is the fraction of porosity. Other constants are explained below.

Salak et al. [4] evaluated the ultimate tensile strength–porosity relationship of over 800 iron compacts from his own experiments and those in the literature and developed an equation based on a best fit line of experimental data. In doing so, a wide variety of pore sizes and shapes as well as microstructures were examined. He found that this best fit line was solved by using a stress intensity factor of 4.3 and reported the ultimate tensile strength of porous iron compacts as follows:

$$\sigma = \sigma_0 e^{-4.3p}$$

Due to wide variation in strength amongst similar porosity levels, the relationship is only representative of the mean best fit and at best provides an approximation of the predicted strength. Therefore, the stress intensity factor is expected to vary amongst different materials depending on the nature of their porosity. A generalized form of this relationship is also reported in the literature without specifying an absolute value for the stress intensity factor, K [5,10], though other empirical studies of sintered steels have found this value to be 10 [10]. The wide variation in the stress concentration factor indicates that this factor is a function of pore shape and pore size in addition to total porosity.

Troshchenko [6] considered the effect of porosity in reducing the load bearing cross-sectional area and formulated the following equation to predict the strength of porous sintered materials:

$$\sigma = \sigma_0\frac{(1 - ap)}{(1 + \beta a)}$$

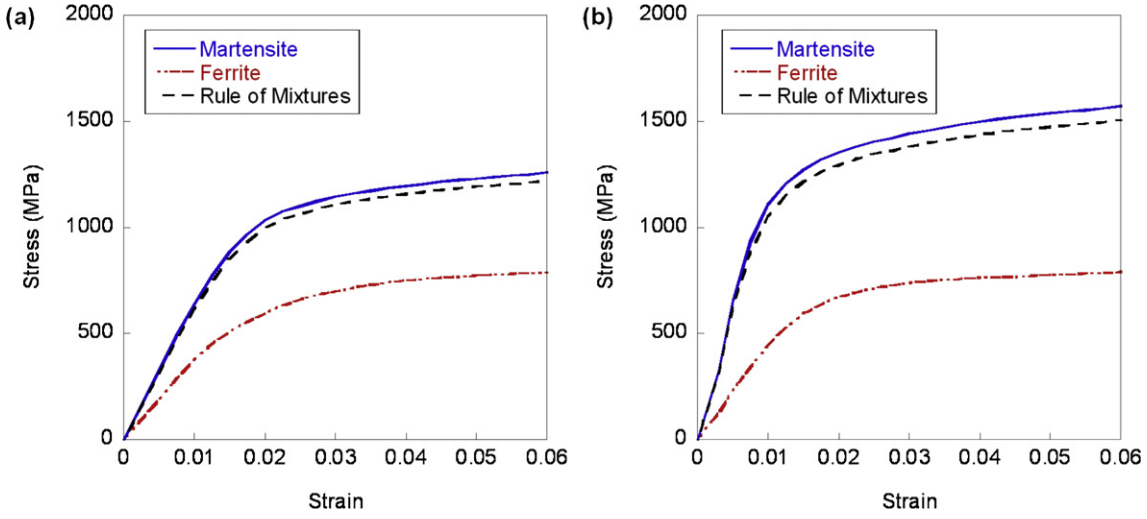

Fig. 6. Average ferrite and martensite curves from micropillar compression with calculated rule of mixtures curves using 8% ferrite and 92% martensite of: (a) as sintered and (b) aged at 538 °C specimens.

where β describes the non-uniformity of the stress distribution across the cross-section and a represents the surface area of the pores. For sintered iron powders, Troshchenko found good correlation to experimental data using β as 2 and a as1.5 times the fractional porosity ($a = 1.5p$).

Haynes [7] developed a strength–porosity relationship by taking into account stress-intensification by pores and implementing a factor, b, which is dependent upon a pore sensitivity factor, K_p:

$$\sigma = \sigma_0 \frac{1-p}{1+bp}$$

$$b = a(K_p - 1)$$

Experimental data for a variety of steels most closely matched theoretical values using b values between 2 and 5, where b increases with decreasing ductility. Again, only a range of strengths was able to be predicted due to variation in mechanical properties of various steels. For the current study of aged steel, where ductility is expected to be low, we therefore use b equal to 4 as a reference.

Fleck and Smith [8] investigated both variable morphology and simple brick models to incorporate the effect of microstructure into a strength–porosity relationship. We focus our attention on the simple brick model here. In this model, pores and particles may be represented by a randomly arranged layered array of cubes where the probability of the existence of a pore is given by $p^{2/3}$ and the probability of the existence of particle is $(1-p^{2/3})$. Furthermore, the probability of the failure plane occurring between two solid particles is $(1-p^{2/3})^2$ and the strength of the sintered material is proportional to this component as follows:

$$\sigma = \sigma_0 (1 - p^{2/3})^2$$

Though the stress concentrating effect due to pore geometry is ignored, Fleck found reasonable agreement to experimental values of sintered steel by applying this model.

These strength–porosity models were applied to the fracture strengths from the aforementioned rule of mixtures analyses of the micropillar compression of ferrite and martensite. The resulting composite strengths which are, thus, inclusive of porosity were then compared to the ultimate tensile strengths from tensile tests of the bulk composite steel and reasonable agreement was found (Table 4). This agreement validates the approach of micropillar compression to determine the strength of individual microconstituents as a basis of predicting the overall material behavior.

Table 4
Comparison of ultimate tensile strength (MPa) from tensile testing and calculated tensile strength (MPa) from micropillar compression.

	As-sintered	Aged at 538 °C
Tensile test	509	588
Salak Model [4]	445	554
Troshchenko Model [6]	467	581
Haynes Model [7]	498	621
Fleck and Smith Model [8]	481	600

Variations in the tensile experimental data and the results from the application of the various porosity–strength relationships may be explained by oversimplifications in the models regarding pore size, shape, orientation, and distribution as well as the non-uniformity of stress distribution due to the stress concentration effect of pores and variations in microstructure. In addition, many of these models neglect the effects of changes in the size and shape of pores as well as the formation of new pores and microcracks during deformation. Previous experimental results also show wide variations in strength at constant porosity [4] indicating that at best these models may only estimate a range of strengths for a given porosity. Furthermore, many of the relationships have only been modeled over discrete ranges of porosity and therefore may not be applicable for the porosity levels examined here.

4. Conclusions

In this study, micropillar compression experiments of ferrite and martensite in dual phase precipitation hardened steel were conducted and the overall bulk behavior was predicted based on the constitutive behavior of the microscopic phases. The following conclusions were drawn:

1. Increased yield and tensile strengths of the bulk steel were observed with aging and were attributed to precipitation hardening from the presence of copper and relief of internal stress from carbon diffusion and tempering of the martensite.
2. Micropillar compression tests showed higher strengths for martensite than ferrite. The ferrite tests exhibit increased yield stress and nearly constant fracture stress with aging. Martensite, however, showed both increased yield and fracture stress with aging, which is consistent with tensile testing results. Due to this

fact and martensite's high phase fraction (92%), martensite is the primary driver to increased strength in the bulk composite steel.
3. Due to the high martensite fraction, a conventional rule of mixtures approach was applied to micropillar compression results of the individual microconstituents to calculate the fracture strengths for the composite steels. The effect of porosity was also incorporated and this resulted in reasonable agreement with the ultimate tensile strengths from tensile tests of the dual phase steels.

Acknowledgement

The authors acknowledge Hoeganaes Corporation for providing the materials and financial support for this research.

References

[1] Introducing Powder Metallurgy (PM), www.mpif.org.
[2] R.J. Boucier, D.A. Koss, R.E. Smelser, O. Richmond, Acta Metall. 34 (12) (1986) 2443–2453.
[3] G. Straffelini, Powder Metall. 48 (2) (2005) 189–192.
[4] A. Salak, V. Miskovic, E. Dudrova, E. Rudnayova, Powder Metall. Int. 3 (1974) 128–132.
[5] E. Klar, P. Samal, Powder Metallurgy Stainless Steels, Processing, Microstructures, and Properties, ASM International, Materials Park, OH, 2007.
[6] V.T. Troshchenko, Poroshkovaya Metall. 3 (15) (1963) 3–11.
[7] R. Haynes, Powder Metall. 14 (27) (1971) 64–70.
[8] N.A. Fleck, R.A. Smith, Powder Metall. 24 (3) (1981) 126–130.
[9] P.S. Liu, C. Fu, T. Li, Trans. Nonferrous Met. Soc. China 9 (1) (1999) 70–78.
[10] H.E. Exner, D. Pohl, Powder Metall. Int. 10 (4) (1978) 193–196.
[11] M. Eudier, Powder Metall. 9 (1962) 278.
[12] C.T. Schade, T.F. Murphy, A. Lawley, R. Doherty, Int. J. Powder Metall. 45 (1) (2009) 38–46.
[13] H.J. Klaar, I.A. El-Sesy, A.H.A. Hussein, Steel Res. 61 (2) (1990) 85–92.
[14] B. Grushko, B.Z. Weiss, Scripta Metall. 23 (1989) 865–870.
[15] D.K. Matlock, G. Krauss, L. Ramos, G.S. Huppi, Structure and Properties of Dual-Phase Steels, American Institute of Mining, Metallurgical, and Petroleum Engineers, 1979, pp. 62–90.
[16] M. Erdogan, R. Priestner, Mater. Sci. Technol. 15 (1999) 1273–1284.
[17] M.S. Rashid, Annu. Rev. Mater. Sci. 11 (1981) 245–266.
[18] G.R. Speich, R.L. Miller, Structure and Properties of Dual-Phase Steels, American Institute of Mining, Metallurgical, and Petroleum Engineers, 1979, pp. 145–182.
[19] I. Tamura, Y. Tomota, M. Ozawa, Proceedings 3rd Intl Conf on the Strength of Metals and Alloys, vol. 1, Cambridge, 1973, p. 611.
[20] P.R. Rios, J.R.C. Guimarães, K.K. Chawla, Scripta Metall. 15 (1981) 899–904.
[21] M. Delince, P.J. Jacques, T. Pardoen, Acta Mater. 54 (2006) 3395–3404.
[22] V.H.B. Hernandez, S.K. Panda, Y. Okita, N.Y. Zhou, J. Mater. Sci. 45 (2010) 1638–1647.
[23] V.H.B. Hernandez, S.K. Panda, M.L Kuntz, Y. Zhou, Mater. Lett. 64 (2010) 207–210.
[24] J.L. Stewart, J.J. Williams, N. Chawla, Metall. Mater. Trans. (2011) in press.
[25] W.D. Nix, H. Gao, J. Mech. Phys. Solids 46 (1998) 411–425.
[26] M.D. Uchic, D.M. Dimiduk, J.N. Florando, W.D. Nix, Science 305 (2004) 986–989.
[27] M.D. Uchic, D.M. Dimiduk, Mater. Sci. Eng. A 400–401 (2005) 268–278.
[28] J.R. Greer, W.C. Oliver, W.D. Nix, Acta Mater. 53 (2005) 1821–1830.
[29] J.R. Greer, W.D. Nix, Appl. Phys. A 80 (2005) 1625–1629.
[30] C. Motz, T. Schöberl, R. Pippan, Acta Mater. 53 (2005) 4269–4279.
[31] W.D. Nix, J.R. Greer, G. Feng, E.T. Lilleodden, Thin Solid Films 515 (2007) 3152–3157.
[32] C.P. Frick, B.G. Clark, S. Orso, A.S. Schneider, E. Arzt, Mater. Sci. Eng. A 489 (2008) 319–329.
[33] A.S. Schneider, B.G. Clark, P.A. Gruber, E. Arzt, Mater. Sci. Eng. A 508 (2009) 241–246.
[34] L. Jiang, N. Chawla, Scripta Mater. 63 (2010) 480–483.
[35] M.A. Pouchon, J. Chen, R. Ghisleni, J. Michler, W. Hoffelner, Exp. Mech. 50 (2010) 79–84.
[36] G.F. Vander Voort, G.M. Lucas, E.P. Manilova, Metallography, Microstructures of Stainless Steels and Maraging Steels, vol. 9, ASM Handbook, 2004, pp. 670–700.
[37] H. Bei, S. Shim, M.K. Miller, G.M. Pharr, E.P. George, Appl. Phys. Lett. 91 (2007) 111915.
[38] W.C. Oliver, G.M. Pharr, J. Mater. Res. 7 (1992) 1564.
[39] R.E. Reed-Hill, R. Abbaschian, Physical Metallurgy Principles, 3rd ed., PWS Publishing Company, Boston, MA, 1994.
[40] S.K. Dhua, A. Ray, D.S. Sarma, Mater. Sci. Eng. A 318 (2001) 197–210.
[41] S.K. Ghosh, A. Haldar, P.P. Chattopadhyay, J. Mater. Sci. 44 (2009) 580–590.
[42] J. Holmes, R.A. Queeney, Powder Metall. 28 (1985) 231.
[43] K.M. Vedula, R.W. Heckel, Modern Developments in Powder Metallurgy, Metal Powder Industries Federation, Princeton, NJ, 1981.
[44] N. Chawla, X. Deng, Mater. Sci. Eng. A 390 (2005) 98–112.
[45] A. Hadrboletz, B. Weiss, Int. Mater. Rev. 42 (1997) 1–44.
[46] S.J. Polasik, J.J. Williams, N. Chawla, Metall. Mater. Trans. A 33A (2002) 73.
[47] D.R.P. Singh, N. Chawla, G. Tang, Y.-L. Shen, Acta Mater. 58 (2010) 6628–6636.